Faraday Discuss., 1992, **94**, 1–22

Introductory Lecture
Studies of the Liquid/Solid Interface by Scanning Tunnelling Microscopy and Scanning Electrochemical Microscopy

Allen J. Bard and Fu-Ren Fan

The University of Texas at Austin, Austin, TX 78712, USA

The application of scanning tunnelling microscopy (STM) and scanning electrochemical microscopy (SECM) to studies of the liquid/solid interface, especially electrode surfaces, is reviewed. Some general principles describing features of the images obtained by these techniques are proposed and illustrated by examples taken from recent work in the authors' laboratory.

Many important and interesting processes occur at the liquid/solid interface; typical examples include the corrosion of metals, the etching of semiconductors, electrodeposition of metals and the dissolution of minerals. Liquid/solid interfaces have long been studied by scientists in an effort to learn about the structure of the interface and the dynamics of reactions in the interfacial region as well as to devise methods for modifying the interfacial structure and its behaviour. For example, an enormous effort is devoted to studies of corrosion and the ways to inhibit it. In the past, methods for studying the interface have largely been macroscopic ones, such as electrochemical perturbation methods.[1] While such methods have been very useful in elucidating the nature of interfaces and the processes that occur in the interfacial region, information about the structure obtained from such methods is largely based on models that attempt to account for macroscopic parameters, *e.g.* the double-layer capacitance, in terms of atomic and molecular structure. Methods that provide more direct structural and compositional information, such as X-ray photoelectron spectroscopy (XPS) and low-energy electron diffraction (LEED), are ultrahigh vacuum (UHV) techniques that require transfer of the interface (emersion) from the liquid environment into UHV.[2,3] Even these techniques produce structural or compositional data that are averaged over rather large areas. However, recent advances have made possible the direct examination of the liquid/solid interface, often with atomic resolution. For example, techniques like *in situ* X-ray diffraction and scanning tunnelling microscopy (STM) have already been applied to the electrode/electrolyte interface. In addition, methods are emerging that allow the study of rapid interfacial reactions (*e.g.* heterogeneous electron transfers) and homogeneous reactions that occur in this region. Finally, means of modification of interfaces and producing designed structures with high resolution have been described; these will play a role in the field of nanotechnology. Thus consideration of the liquid/solid interface at high resolution encompasses structural characterization, dynamic measurements and fabrication.

The interface between a solid and liquid actually constitutes a region of finite thickness where the properties are different than those of the bulk phases (Fig. 1). While the actual 'interface' may only consist of the top layer of surface atoms of the solid, as well as specifically adsorbed species in contact with the liquid phase, this interface can perturb the nearby liquid phase, for example, because of the electrical effects of surface charges. The distribution of carriers (electrons and holes) in a solid near the interface can also be perturbed by surface charges, with the formation of a space-charge region in a lightly or moderately doped semiconductor.

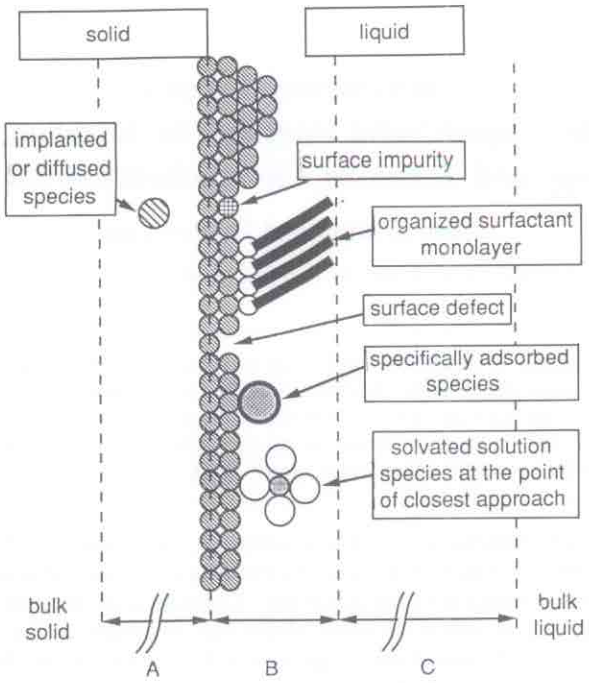

Fig. 1 Schematic representation of the liquid/solid interfacial region showing possible species and features. A, Space-charge region (10^{-10}–10^{-6} m), bulk solid atoms and carriers (electrons and holes) not shown. B, Surface region with adsorbed molecules and monolayer films (*ca.* 2–20 Å). C, Region of diffuse-layer and modifying films (10^{-9}–10^{-6} m), solvent molecules not shown

The distribution of surface states at the interface (representing, for example, lattice defects, adsorbants or lattice impurities) and near-surface species introduced by ion implantation or diffusion, may also be important in understanding interfacial behaviour. Thus a complete description of the liquid/solid interface requires consideration of the composition, structure and electrical properties of a thicker zone, the interfacial region.

We discuss here the application of two complementary techniques, scanning tunnelling microscopy (STM) and scanning electrochemical microscopy (SECM), to liquid/solid interfacial studies. STM produces, in favourable cases, atomically resolved images of the electron distribution at conductor and semiconductor surfaces, and through a related technique, tunnelling spectroscopy (TS), information about energy levels at the interface. STM is not useful with insulators, although a related technique, atomic force microscopy (AFM), can be employed to obtain high-resolution topographic images with these. STM is also not very useful in learning about the chemical nature of the interface nor in studying reactions in this region, although it can be used to observe changes of surface structure with time and potential. SECM is a lower resolution technique (currently down to about the 30 nm level), but it can be used with all types of surfaces and can be chemically selective. Several different applications of STM (and TS) and SECM are given to illustrate their usefulness in studies of interfaces.

Scanning Tunnelling Microscopy

At the outset, it might be useful to summarize some general features of the interface that have already emerged from STM studies. These will be discussed in connection

with the examples that follow: (1) surfaces, even 'well defined' single-crystal surfaces, are rarely atomically smooth, except over small areas. Instead they are characterized by step edges, defects and other features that can behave as active sites in surface reactions. Sites of this type are frequently not discernable by diffraction techniques like LEED. (2) Surface atoms are often mobile, so that surfaces reconstruct and change with time. (3) The STM tip can interact strongly with surface species, depending on the selected tunnelling parameters. Thus adsorbed species, especially if not arranged in a 'tight-packed' structure, can be pushed along the surface by the scanning tip. (4) In interpreting STM images, it is important to realize that the STM does not image atoms, but rather shows electronic distributions.

Surface Structures of Single Crystals

Considerable progress has been made over the past few years toward the application of STM to the study of surface structures of many materials including metals, carbon and semiconductors. Generally, single crystals with different orientations or layers with ordered structures have been studied.

Metals

Various metals including Pt,[4,5] Rh,[6] Ag,[7,8] Ni,[9] Au,[10,11] and epitaxially grown thin films of Au[12,13] have been investigated by STM with atomic resolution. Very recently, the surface reconstruction of metals in solution has also been revealed by *in situ* STM studies. For example, Gao *et al.*[14,15] reported that the Au(110) 1×1 structure transformed to a 1×2 structure in the double-layer region, when the electrode potential was lowered to -0.3 V *vs.* SCE in $HClO_4$ solution.

Carbon

Carbon electrodes are widely used in electroanalysis, organic electrosynthesis and fuel cells. Highly oriented pyrolytic graphite (HOPG) is of particular interest and widely used as the substrate for STM studies because of its easily renewable and atomically flat surface and well defined structure.[16–18] However, in addition to atomically smooth plateaux, many different structures can also be observed on freshly cleaved HOPG surfaces. For example, strands, fibres, fibre clusters, flakes and broken pieces are occasionally observed by STM. These structures cover as much as 1–10 % of the total HOPG surface area.[18] Thus when HOPG is used as a substrate for STM imaging, one must be cautious in distinguishing these graphite structures on HOPG from those attributed to supported species. Recently, Chang *et al.*[19,20] reported a technique for the formation of monolayer pits of controlled, uniform, nanometer size on HOPG by gasification reactions. These pits serve as markers and nucleation sites, so that pitted HOPG (as shown in Fig. 2) is useful for both STM and electrochemical studies (as discussed below).

Semiconductors

Semiconductor surfaces can be studied by STM, and the related techniques tunnelling spectroscopy (TS) and scanning tunnelling spectroscopy (STS) in gaseous or liquid environments, *e.g.* n-TiO_2,[21–24] n-ZnO,[25] GaAs,[26–28] n-FeS_2,[29] Si,[30–36] and transition-metal dichalcogenides.[37] The atomic image of a Si(111) surface can be obtained in solutions.[33,34] As shown in Fig. 3A, a long-range ordered structure can be imaged in 1% HF after the Si(111) surface is pretreated with a mixed solution of H_2O_2 and HF. Several

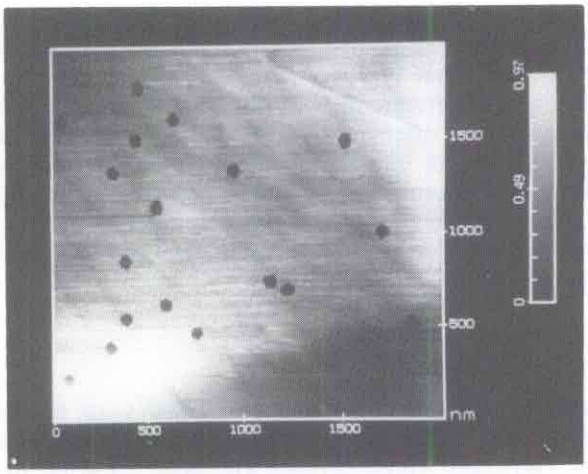

Fig. 2 STM image of pits formed on HOPG by heating in air at 650 °C for 15 min. These pits are of monolayer depth with a diameter governed by time of heating. Reprinted with permission from ref. 19. Copyright 1990 American Chemical Society

atomically flat terraces appear that are separated by monoatomic steps intersecting in a sawtooth pattern. This surface feature has been attributed to the surface misorientation of the Si sample to the structures of the steps.[32] An enlarged atomic image of the Si(111) surface is shown in Fig. 3B. This ordered structure, similar to that observed by STM in UHV[35] and by AFM in air,[36] is attributed to the Si(111) 1×1 H phase, with a nearest atomic spacing of 0.38 ± 0.02 nm.

In addition to imaging, TS and STS studies have been performed on several semiconductors.[29,38,39] Two types of TS measurements can be made with the tip held fixed at a given position above the substrate surface. In current–voltage (I–V) measurements, the current is recorded as a function of the bias voltage between sample and tip. In conductance ($\mathrm{d}I/\mathrm{d}V$)–voltage measurements, the magnitude of a 10 kHz modulation in-phase current is recorded as a function of voltage. Such conductance measurements reveal electron tunnelling into the conduction band and from the valence band of the semiconductor to the tip, as shown in the energy band diagram of an ideal n-type MIS structure (Fig. 4). Fig. 5(a) shows a typical conductance ($\mathrm{d}I/\mathrm{d}V$) spectrum for a heavily doped (*ca.* 2.7×10^{18} cm^{-3} doping density) n-FeS_2 (001) surface in air over a bias voltage range of -1.8 to $+1.8$ V (substrate *vs.* tip). As shown, there is a wide region of low conductance terminating at both ends in regions of sharply rising conductance. The normalized conductance, obtained by dividing the differential conductance ($\mathrm{d}I/\mathrm{d}V$) by the integral conductance (I/V), is shown in Fig. 5(b). In the positive-bias region, the normalized conductance shows a broad peak of width *ca.* 1.5 eV† with several fine features superimposed; this has tentatively been attributed to the result of electron transfer between the tip and a broad delocalized surface state. In the negative-bias region the spectrum shows a narrow peak ($\geq$0.5 eV wide) centred *ca.* -1.6 V, which is superimposed on a high increasing background. This narrow peak has been attributed to electron transfer between the tip and the fairly localized uppermost valence level consisting mainly of Fe 3d t_{2g} states. TS studies of surface immersed in liquids are more difficult because a large Faradaic a.c. current flows in addition to the tunnelling current, even at insulated tips.

† 1 eV $\approx 1.602\,18 \times 10^{-19}$ J.

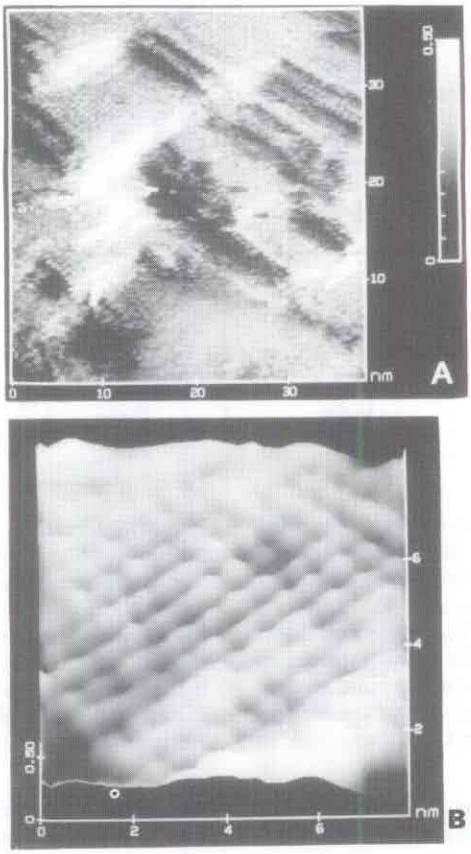

Fig. 3 A, *In situ* STM atomic resolution of hydrogen-terminated Si(111) in 1 % HF solution. The Si(111) sample was pretreated with alcohol and triply distilled water, followed by chemical etching in dilute H_2O_2 and HF before it was mounted in the STM cell. Thermal drift and error in the calibration of the piezo cause some distortion of the image. The potential of Si and the W tip were −0.95 and −0.35 V, respectively. B, Higher-resolution three-dimensional view of the atomic arrangement. This image was subjected to a two-dimensional Fourier-transform filter which removed high-frequency noise equivalent to a distance below 0.30 nm. Reprinted with permission from ref. 33. Copyright 1992 The Electrochemical Society

Adsorbed Species on Single Crystals

STM has also been successful in imaging adsorbed species, especially those that pack in an ordered arrangement on the surface thereby minimizing adsorbate movement caused by interactions with the tip.

Underpotential Deposition

The electrochemical deposition of metals is known to occur generally *via* a nucleation and growth mechanism and is one of the most structure-sensitive reactions.[40] When a metal is deposited onto a foreign substrate rather than on a surface of its own kind, a monolayer is often deposited at potentials more positive than the reversible potential of the bulk phase. This underpotential deposition (UPD) is equivalent to the adsorption of metal atoms on a substrate surface. STM has been applied to UPD studies of Pb on Au(111)[41] and Ag(100)[7] as well as Cu on Pt(111)[42] and Au(111).[43,44]

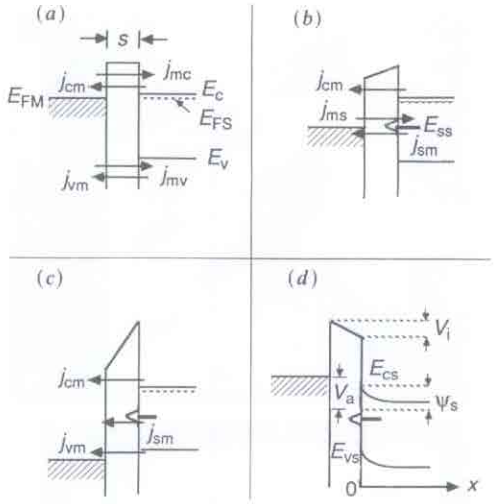

Fig. 4 (*a*) Energy-band diagram of an ideal n-type MIS structure defining the four current components *via* the enegy bands of the semiconductor $V_a = 0$. (*b*), (*c*) and (*d*) are the energy-band diagrams for n-type MIS structures showing potential distribution under different bias conditions. (*b*) $V_A < 0$, $E_{FM} = E_{ss} > E_{vs}$; (*c*) $V_a < 0$, $E_{FM} \leqslant E_{vs}$; (*d*) $V_a > 0$, $E_{FM} > E_{cs}$. E_{FM} is the Fermi level in the bulk of the metal; E_{FS} is the Fermi level of the semiconductor in the bulk; E_c and E_v are the CB and VB edges of the semiconductor in the bulk; E_{cs} and E_{vs} are the corresponding values at the surface. E_{ss} is the surface state energy; V_a is the applied voltage; V_i is the voltage drop across the insulator and ψ_s is the semiconductor surface potential. Reprinted with permission from ref. 29. Copyright 1991 American Chemical Society

The UPD of Cu on Au(111) has also been recently investigated using AFM by Manne *et al.*[45] AFM images taken at +0.7 V *vs.* a Cu wire in either 0.1 mol dm^{-3} $HClO_4$ or 0.1 mol dm^{-3} H_2SO_4 containing 1 mmol dm^{-3} Cu^{2+} prior to Cu deposition showed large areas exhibiting Au(111) atomic resolution (Fig. 6A). When the potential was swept to −0.100 V at 10 mV s^{-1} to initiate bulk Cu deposition, the surface structure quickly (*ca.* 10 s) settled into images of a close-packed surface with interatomic distance of 0.26 ± 0.02 nm (Fig. 6B). Sweeping the potential to 0.110 V removed the bulk-deposited Cu but left the UPD monolayer in place. Here, different images were found in different electrolytes. In perchloric acid, images appeared with the same spacing (0.29 ± 0.02 nm) found for the Au(111) surface at +0.7 V (Fig. 6C). However, the lattice direction was rotated by 30 ± 10° relative to the underlying Au lattice. The Cu adatoms are arranged in an incommensurate fashion with respect to the Au(111) surface (Fig. 6D). In sulfuric acid, a $(\sqrt{3} \times \sqrt{3})$R30° overlayer structure was observed (Fig. 6E and F). The distance of the nearest neighbours of Cu adatoms is 0.49 ± 0.02 nm and the atomic rows of Cu are rotated 30 ± 10° relative to the underlying Au lattice. This $(\sqrt{3} \times \sqrt{3})$R30° structure has also been found by STM.[43,44]

Adsorbents, Monolayers and Organic Films

Recently, STM has been used to study adsorbates[46–48] or organic monolayers formed by self-assembly.[49–53] For example, Yau *et al.*[5,46] demonstrated the imaging of iodine on Pt(111) in air or an electrochemical environment with atomic resolution, relying on non-vacuum preparation techniques. *In situ* STM combined with IR spectroscopy has been employed to characterize the CO adlayer on Rh(111) and Pt(100) electrodes in aqueous solution.[47,48] McCarley and Bard[54] reported atomically resolved STM images of iodide adsorbed on Au(111). Shown in Fig. 7A is an atomically resolved Au(111)

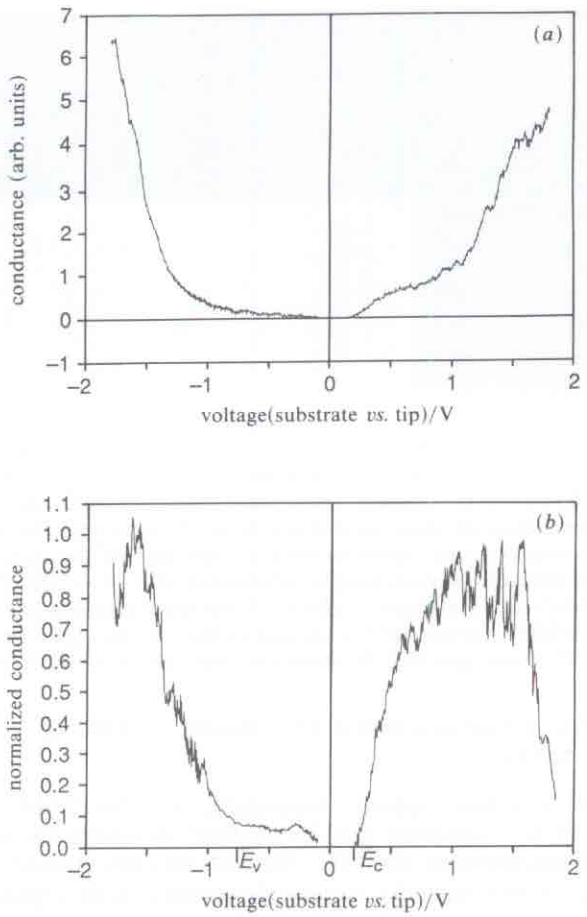

Fig. 5 (*a*) Conductance (dI/dV) as a function of voltage for an Ir–Pt tip and n-FeS_2 sample. Modulation frequency of 10 kHz and modulation amplitude of 20 mV peak-to-peak were employed in the phase-sensitive technique. (*b*) Normalized conductance $(dI/dV)/(I/V)$ as a function of bias voltage. Reprinted with permission from ref. 29. Copyright 1991 American Chemical Society

surface imaged in air by STM. The hexagonal arrays in the image are characteristic of Au(111) with a measured periodic spacing of 0.29 ± 0.02 nm. An STM image of an Au substrate treated with KI solutions (10^{-5}–10^{-2} mol dm^{-3}) is shown in Fig. 7B. The nearest-neighbour and next-nearest-neighbour spacings of the periodic structure are 0.50 ± 0.03 and 0.88 ± 0.05 nm, respectively. These spacings are consistent with the $(\sqrt{3} \times \sqrt{3})$R30° adlayer structure previously reported by LEED studies.[55] Fig. 7C shows direct evidence for the adlayer structure obtained near an iodide/Au–bare Au domain boundary. Clearly shown in this figure are the rotation ($30° \pm 2°$) and the spacing of the adsorbate unit cell with respect to the underlying Au(111) substrate.

Atomic resolution STM images of Au(111) treated with sulfide or thiocyanate display patterns of atoms in the shape of squares with nearest-neighbour distances of 0.27 ± 0.03 nm.[56] The square pattern observed is ascribed to images of Au atoms on a reconstructed Au(111) surface caused by dissolution of Au by sulfide or thiocyanate. This finding is consistent with quartz-crystal microbalance studies which demonstrate that Au dissolves in aqueous solutions of sulfide and thiocyanate with O_2 present.

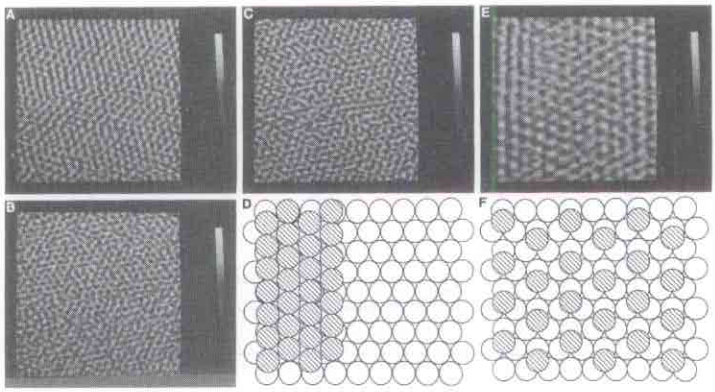

Fig. 6 AFM images (6 nm × 6 nm) of a Au(111) electrode surface in electrolyte and 10^{-3} mol dm^{-3} Cu^{2+} under potential control at different voltages. A, $V = +0.7$ V showing Au(111) corrugation. B, Bulk-deposited Cu at −0.1 V. The atom–atom distance is 0.26 nm. C, Close-packed overlayer of Cu observed at +0.114 V in 0.1 mol dm^{-3} perchloric acid. The atom–atom distance is 0.29 nm. D, Schematic of incommensurate close-packed overlayer of Cu on Au. The open circles represent Au atoms, while the striped circles represent the Cu. Only part of the monolayer is exhibited in order to demonstrate the overlayer–underlayer orientation. E, $(\sqrt{3}\times\sqrt{3})$R30° overlayer of Cu on Au observed at +0.144 V in 0.1 mol dm^{-3} sulfate. Atom–atom distance is 0.49 nm. F, Schematic representing $(\sqrt{3}\times\sqrt{3})$R30° overlayer of Cu (striped circles) on Au (open circles). Reprinted with permission from ref. 45. Copyright 1991 the American Association for the Advancement of Science

Ordered Structures of Self-assembled Monolayers (SAM) of Organothiols on Au(111)

The $(\sqrt{3}\times\sqrt{3})$R30° structure appears frequently, *e.g.* for SAM on Au(111). For example, Widrig *et al.*[49] reported a $(\sqrt{3}\times\sqrt{3})$R30° structure for ethanethiolate and octadecanethiolate adsorbed on Au(111). We also recently studied ordered structures obtained by STM on the Au(111) surface derivatized with organothiols of various sizes {4-aminothiophenol (4-ATP); $[Ru(bpy)_2$ (4′-(12-mercaptododecyl)-4-methyl-2,2′-bipyridine)$](PF_6)_2$ (abbreviated Rub_2b^*); $(C_5H_5)Fe(C_5H_4CO_2[CH_2]_{16}SH$; pentaammine([2]staffane-3,3′-dithiol)ruthenium(II) $(PF_6)_2$ (abbreviated as Ru-[2]S-thiol)}.[57] The structures of these organothiols, some of which are too large to pack in a $(\sqrt{3}\times\sqrt{3})$R30° pattern are shown in Fig. 8.

Fig. 9A is an STM image of a 4-ATP modified Au(111) surface, showing a nearest-neighbour spacing of 0.49 ± 0.03 nm and a next-nearest-neighbour spacing of 0.89 ± 0.05 nm. This spacing is consistent with a $(\sqrt{3}\times\sqrt{3})$R30° structure and a maximum coverage (θ) of 1/3. The two-dimensional Fourier spectrum of the raw data (Fig. 9B) indicates that the $(\sqrt{3}\times\sqrt{3})$R30° structure is the only discernible structure. The maximum surface coverage obtained by STM (0.33) agreed quite well with the coverage determined electrochemically from the integrated charge under the oxidation peak of the cyclic voltammogram corresponding to the oxidation of the aniline moiety, assuming a roughness factor of 1.0 to 1.5 for the Au-mica electrode.

Unfiltered, constant-height images of a Au(111) surface modified with Rub_2b^* are displayed in Fig. 10. As seen in the two-dimensional Fourier transform of the image in Fig. 10B (Fig. 10D), there appears to be only one spacing of ordered species. The nearest- and next-nearest-neighbour spacings are again 0.51 ± 0.03 and 0.87 ± 0.05 nm, characteristic of a $(\sqrt{3}\times\sqrt{3})$R30° structure. However, a spacing of 0.51 nm is much smaller than the physical dimension of the Rub_2b^* (its ω-substituent has a dimension of *ca.* 1.3 nm). Similarly, the ferrocene ω-substituted thiol, $(C_5H_5)Fe(C_5H_4(CO_2(CH_2)_{16}SH))$, in which the ferrocene group has a physical dimension

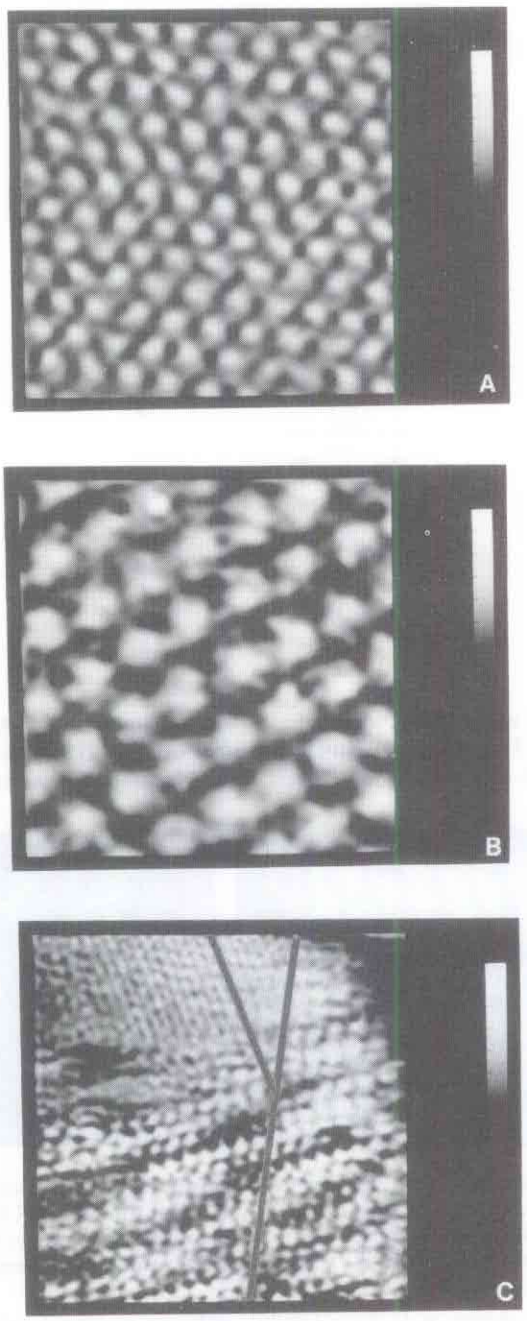

Fig. 7 A, Constant-height image of a 3 nm × 3 nm area of an uncoated Au(111) film; $V_t = 20$ mV; $i_t = 3.0$ nA. The grey scale is 0 to 0.7 nm. B, Constant-height image of a 3 nm × 3 nm area of an iodide-coated Au(111) substrate prepared by dosing in 10^{-2} mol dm^{-3} KI solution for 30 min, $V_t = 50$ mV; $i_t = 1$ nA; $0 \leq z/\text{nm} \leq 1$. The image is uncorrected for thermal drift. C, Constant-height image of a 9.5 nm × 9.5 nm area near an adlattice defect on an Au(111) substrate; $V_t = 20$ mV; $i_t = 3$ nA; $0 \leq z/\text{nm} \leq 1$. Lines show direction of adlattice unit cell with respect to the underlying Au(111). Reprinted with permission from ref. 54. Copyright 1991 American Chemical Society

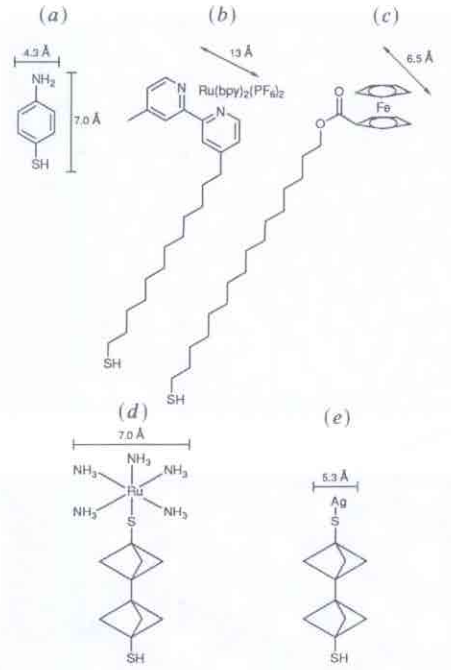

Fig. 8 Structures of organothiols used, (*a*) 4-aminothiophenol (4-ATP), (*b*) Rub_2b^*, (*c*) $(C_5H_5)Fe(C_5H_4CO_2[CH_2]_{16}SH)$, (*d*) Ru-[2]S-dithiol, (*e*) Ag-[2]S-dithiol. Reprinted with permission from ref. 57. Copyright 1992 American Chemical Society

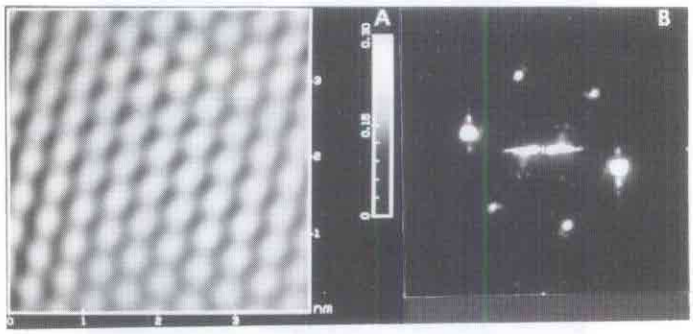

Fig. 9 A, STM image of a 40 Å × 40 Å area of a 4-ATP monolayer film coated on Au(111)–mica. Constant-current mode, $V_b = -31.1$ mV, $I_t = 6.2$ nA. B, Two-dimensional Fourier spectrum of raw data shown in A. The hexagonal pattern was used to construct the image shown in A. Reprinted with permission from ref. 57. Copyright 1992 American Chemical Society

of *ca.* 0.65 nm, also shows a $(\sqrt{3} \times \sqrt{3})R30°$ adlayer structure with the nearest- and next-nearest-neighbour spacing of 0.52 ± 0.03 and 0.89 ± 0.05 nm (Fig. 11). However, electrochemical surface coverage measurements based on the Fc/Fc^+ wave in 1.0 mol dm^{-3} $HClO_4$ ($\theta = 0.15$–0.21) agree well with those predicted by a close-packed model ($\theta = 0.18$), with a sphere diameter of 0.65 nm.

Fig. 12A shows an STM image of a Ru[2]S-dithiol modified Au(111) surface. The corresponding two-dimensional Fourier spectrum (Fig. 12B) indicates two different sets of hexagonal periodicities on the surface. The outer hexagonal structure shows a

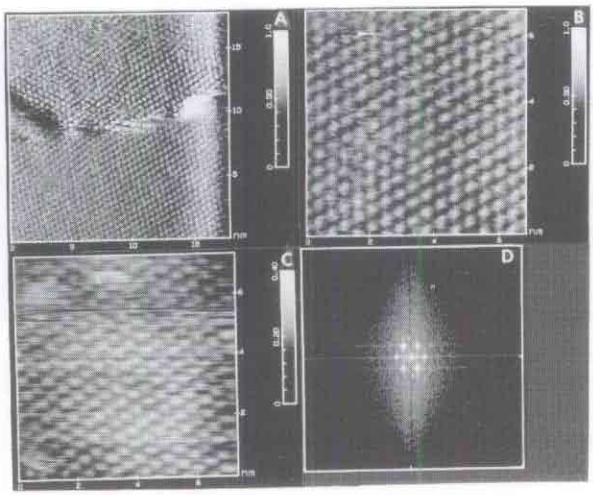

Fig. 10 A and B, Unfiltered, constant-height images of Rub_2b^* adsorbed on Au(111) for two areas on the sample: 225 Å × 225 Å and 70 Å × 70 Å for A and B, respectively. C, Unfiltered, constant-current image of the area in B. $I_t = 1$ nA and $V_b = 20$ mV. D, Two-dimensional Fourier spectrum of raw data in B. Reprinted with permission from ref. 57. Copyright 1992 American Chemical Society

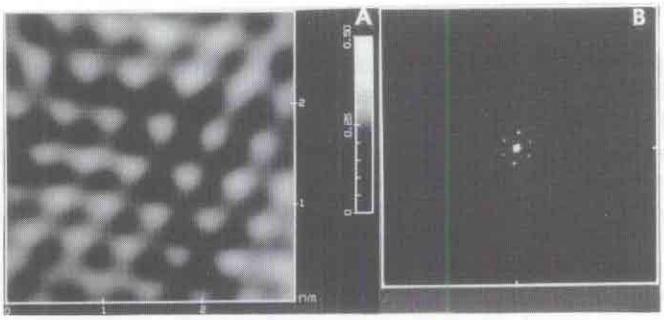

Fig. 11 A, Two-dimensional Fourier-filtered image of $(C_5H_5)Fe(C_5H_4CO_2[CH_2]_{16}SH)$ on Au(111). $I_t = 1$ nA and $V_b = 20$ mV. B, Two-dimensional Fourier spectrum of raw data. Reprinted with permission from ref. 57. Copyright 1992 American Chemical Society

nearest-neighbour spacing of 0.48 ± 0.03 nm and a next-nearest-neighbour spacing of 0.87 ± 0.005 nm, again a $(\sqrt{3} \times \sqrt{3})R30°$ structure. The inner hexagonal set represents a nearest-neighbour spacing of 0.98 ± 0.05 nm and a next-nearest-neighbour spacing of 1.74 ± 0.10 nm, which corresponds to a $2(\sqrt{3} \times \sqrt{3})R30°$ structure. As shown in Fig. 8D, the diameter of the staffane cage is *ca.* 0.53 ± 0.02 nm and that of $Ru(NH_3)_5$ is *ca.* 0.70 ± 0.02 nm, thus the Ru-[2]S-dithiol cannot pack closer than 0.70 nm. The $2(\sqrt{3} \times \sqrt{3})R30°$ structure may be the actual packing arrangement, if the adsorption of Ru-[2]S-dithiol is commensurate with the underlying Au(111).

In conclusion, a $(\sqrt{3} \times \sqrt{3})R30°$ superlattice structure was seen for the adsorption of different-sized thiol compounds, even when the ω-substituent size was so large that such a packing should not be possible. The observed ordered structure suggests that the images are probably caused by the electronic perturbations of the Au(111) surface by the adsorbed thiol. One must remember that the STM does not image atoms, but rather

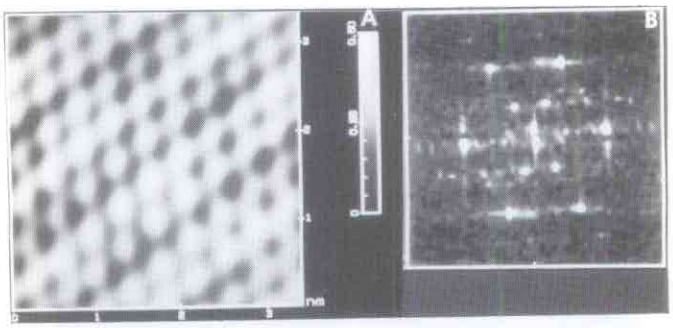

Fig. 12 A, STM image of a 34 Å × 34 Å area of Ru-[2]S-dithiol monolayer film coated on Au(111)–mica. Constant-current mode, $V_b = 200$ mV, $I_t = 0.5$ nA. B, Two-dimensional Fourier spectrum of raw data shown in A. Two distinct hexagonal patterns are clearly observed and used to construct the image shown in A. Reprinted with permission from ref. 57. Copyright 1992 American Chemical Society

the electronic distribution at the interface. Thus adsorbed molecules, in one arrangement can lead to perturbation of the Au(111) electronic distribution to produce a pattern that is different than the actual molecular arrangement on the surface.

Etching of Self-assembled Organothiol Layers on Au(111) *and Tip–Substrate Interaction*

As mentioned previously, the tip can interact with adsorbed molecules. For example, purposeful etching of the self-assembled organothiol monolayers can be achieved by bringing the STM tip close to the substrate using a low bias potential (*e.g.* 10 mV) and a high tunnelling current (*e.g.* 10 nA) or by the application of a high bias potential (*e.g.* 3 V) for a few seconds.[58,59] Fig. 13 shows the selective removal of organothiol surface layers by purposeful etching, *i.e.* an STM image of an *n*-octadecanethiol film on Au before etching (Fig. 13A) and the same area after the STM was used to etch a 10 nm × 10 nm area (as shown by the broken square) for 10 s by scanning this area with a lower tunnelling voltage (10 mV) and a higher tunnelling current (10 nA) (Fig. 13B). The four holes thus produced reveal direct interaction between the tip and the thiol layer. The effect of continuous scanning (*ca.* 10 and *ca.* 35 min) of the same area with normal scanning parameters (1 nA at 1 V) is shown in Fig. 13C and D.

Surface Reactions

Reactions occurring at surfaces can be followed by monitoring changes in surface structures with time or potential using STM. The previously mentioned study of the growth of pits on HOPG during heating in air at 650 °C[19,20] is an example of an *ex situ* approach. This surface was useful for an *in situ* study of the deposition of Pb and HOPG owing to the presence of markers and nucleation sites. Metal deposition or dissolution takes place preferentially at the step edges. Fig. 14A shows an example of the *in situ* Pb deposition on an HOPG substrate which was initially treated to produce monolayer-deep pits.[60] The sequence of images along with substrate potential displayed in this figure shows Pb deposition when the substrate potential is stepped to −600 mV *vs.* SCE and its subsequent stripping when the HOPG potential is returned to the initial potential, −79 mV *vs.* SCE. As clearly shown in these images, Pb is preferentially grown at the step edges of HOPG when the substrate potential is stepped into the Pb deposition

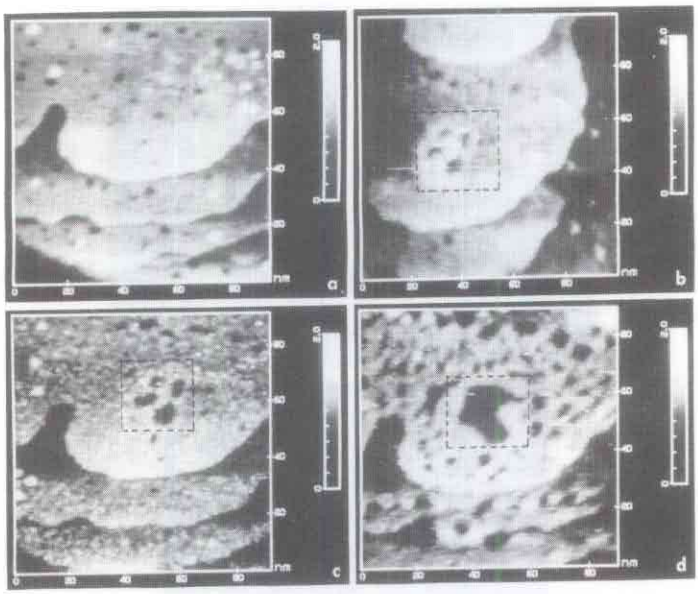

Fig. 13 STM image of a 100 nm × 100 nm of: a, *n*-octadecanethiol film coated on Au-mica; b, same area after 10 s of etching mode ($V_b = 10$ mV, $I_t = 10$ nA) over a 10 nm × 10 nm area (within area shown by broken line); c, same area after 10 min continuous normal scanning; d, after 35 min normal scanning. All images were taken in constant current mode in air, $V_b = +1$ V, $I_t = 1$ nA.
(Reprinted with permission from ref. 58. Copyright 1992 American Chemical Society.)

region. A tip–substrate interaction also occurs here. In Fig. 14B we show an *in situ* STM image of Pb located around edges of pits.[60] Note that the material appearing at the edges of the HOPG pits seems to be more concentrated on the 'downhill' side of the scan. A possible cause is the movement of Pb on the HOPG surface as the tip pushes the metal particles. Streaks seen in this figure are probably due to Pb which has been pushed over the pit edge and along the surface while imaging. One should be aware of other possible tip effects in electrochemical studies. For example, the tip can shield the area directly below it, as is well known from analogous effects found with Luggin capillaries. An even more significant effect arises when the potential applied to the tip affects the potential distribution on the substrate being examined. For example, in the Pb deposition on HOPG study, if the tip potential was too positive, Pb would not deposit below it on the HOPG, although deposition on the remainder of the HOPG surface was clearly seen.

The surface reactions of Au(111) with oxygen in an aqueous cyanide solution can also be studied by *in situ* STM (Fig. 15).[61] At time zero, the surface is already pitted, although the time to place the solution on the Au(111) surface and reassemble the microscope was fairly short, *ca.* 1 min. As shown, the pit sizes did not increase with time, but rather decreased, probably because of depletion of CN^- from the small volume of solution. If more CN^- solution was added, the surface began to dissolve again. The rates of etch-pit annealing (normalized pit circumference *vs.* time) are displayed in Fig. 16 for different CN^- concentrations. As shown, there is no preferred initial trend for pits of different size, but after some induction time, the rates attain a steady value. The rate did not depend on CN^- concentration, but the time to reach this steady rate did depend on CN^- concentration. Effects of surface atom mobility have also been observed in the dealloying of Cu_3Au[62] and Ag–Au alloys,[63] as well as with Au substrates immersed in solutions with or without chloride.[10,12]

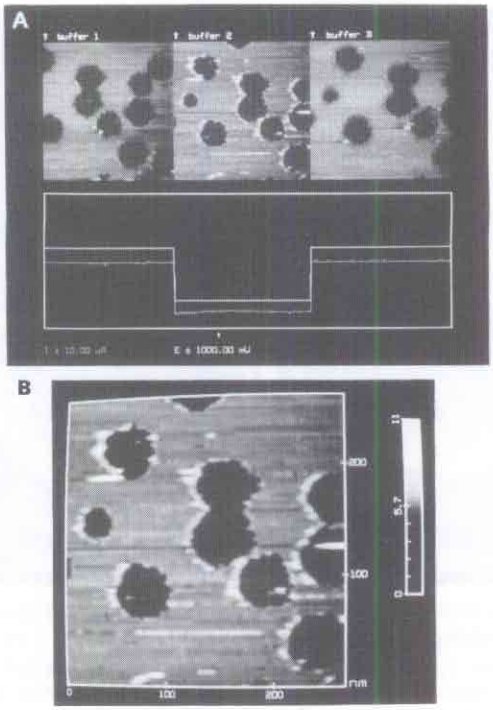

Fig. 14 A, Sequence of three *in situ* STM images with substrate potential showing the subsequent deposition and stripping of Pb on a single area of thermally etched HOPG. Deposition was carried out at −600 mV *vs.* SCE with the tip ramped from 382 to −400 mV and back in 0.5 mmol dm^{-3} $Pb(NO_3)_2$ and 1 mol dm^{-3} $NaClO_4$. B, *In situ* STM images of Pb located around edges of pits. Imaging was done with tip at 382 mV *vs.* reference and a set point current of 5 nA. Reprinted with permission from ref. 60. Copyright 1992 The Electrochemical Society

Fabrication

The utilization of STM and AFM for surface modification has been extensively reviewed by Quate.[64] He concludes that these scanning probes can be used for microfabrication of structures on solid substrates with a resolution that is improved by a factor of ten beyond what is achievable with conventional methods. A few examples of microfabrication with STM in this laboratory involve the purposeful etching of the SAM organothiol films on Au[58,59] and the laser-induced photoetching of CdSe film.[65]

Projections

STM is an important new tool for *in situ* and *ex situ* characterization of electrodes, *e.g.* the imaging of surface structures at scales ranging from submicron to atomic resolution. However, the interpretation of the images observed is still rather qualitative and the confirmation of images from theoretically calculated electron distributions is rarely reported. The STM image itself is also not very useful for learning about the chemical nature of the surface. The related spectroscopic techniques, roughly equivalent to voltammetry, may prove useful, but still need to be developed. Especially when combined with optical methods, STM may be extended to insulating (but photoconductive) or luminescent materials. Finally, a potentially important application of *in situ* STM is as a probe of the liquid side of the (solid/liquid) interface, *e.g.* to map ion or potential distributions near an interface.

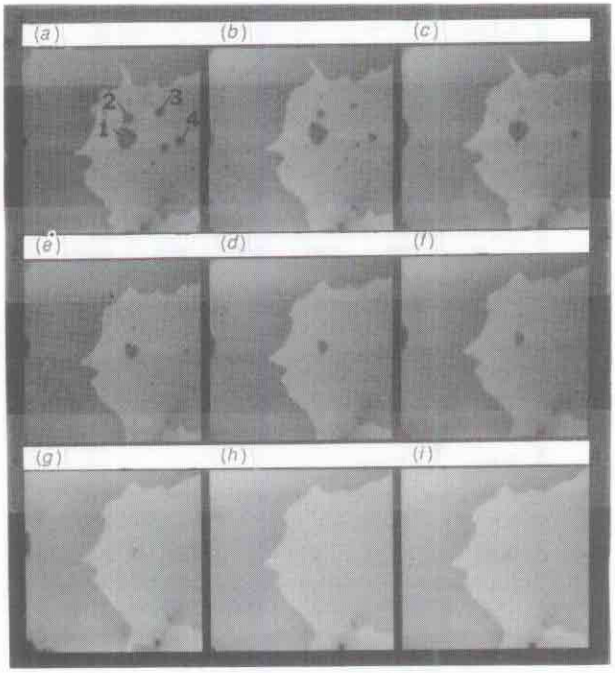

Fig. 15 *In situ* constant-current images at different times for a 200 nm × 200 nm section with $[CN^-] = 5 \times 10^{-5}$ mol dm^{-3}. Image at $t = 0$ s shows pits formed in Au(111) by reaction with CN^- and O_2. After CN^- depletion, pits healed by Au atom movement on surface. Grey scale is 0–5nm. t/s 0 (*a*), 158 (*b*), 306 (*c*), 956 (*d*), 1976 (*e*), 2694 (*f*), 3744 (*g*), 4607 (*h*), 4919 (*i*). Reprinted with permission from ref. 61. Copyright 1992 American Chemical Society

Scanning Electrochemical Microscopy

Overview

SECM, as STM, utilizes small conductive tips (usually ultramicroelectrode disks) that are moved with high resolution by piezoelectric elements near the interface of interest. Several reviews of this technique and earlier related studies have appeared recently,[66–68] so only a brief introduction to the general principles will be given here. In SECM, a redox reaction, *e.g.* $O + ne \rightarrow R$, occurs at an ultramicroelectrode (*i.e.* an electrode with a radius below *ca.* 25 μm) that serves as the working electrode in an electrochemical cell containing species O at a concentration, c^*. A steady-state current, $i_{T,\infty}$ of a magnitude given by

$$i_{T,\infty} = 4nFDc^*a \tag{1}$$

is rapidly attained at an ultramicroelectrode, where D is the diffusion coefficient and a the electrode radius. This expression applies when the tip is distant by several electrode diameters from any surface. When the tip is near a surface, the tip current, i_T, is different from $i_{T,\infty}$ and depends upon the nature of the surface and the distance between tip and surface, d. If the surface is one at which no electron-transfer reactions occur, *e.g.* an electronic insulator, it blocks diffusion of O to the tip, so that $i_T/i_{T,\infty} < 1$. If oxidation of R occurs at the surface, regenerating O, the flux of O to the tip is enhanced, and $i_T/i_{T,\infty} > 1$. The actual current–distance behaviour, most conveniently represented in the dimensionless form of plots of $i_T/i_{T,\infty}$ *vs.* d/a, depends somewhat on the tip shape

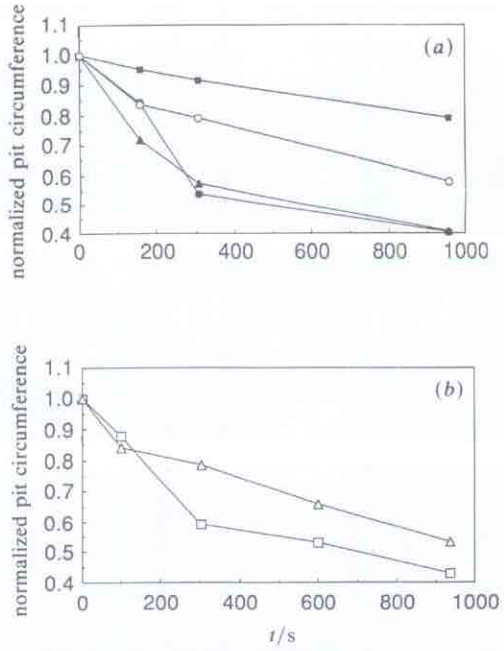

Fig. 16 Pit circumference normalized to initial circumference. (*a*) $[CN^-] = 5 \times 10^{-5}$ mol dm^{-3} (*b*) $[CN^-] = 7.5 \times 10^{-5}$ mol dm^{-3}. Reprinted with permission from ref. 61. Copyright 1992 American Chemical Society

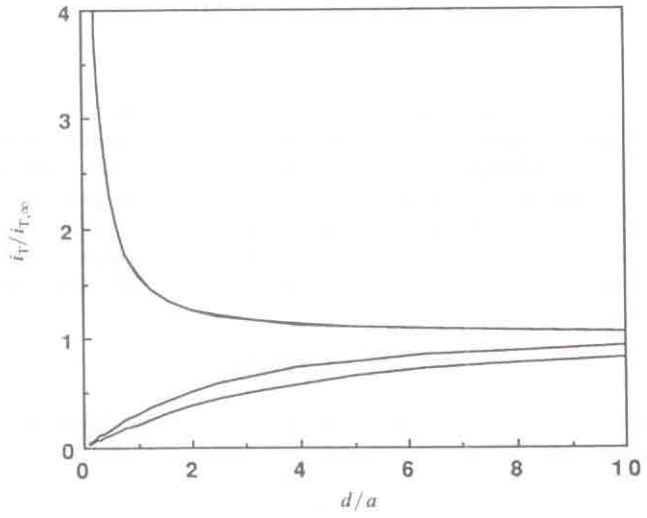

Fig. 17 Plot of i_T normalized with respect to $i_{T,\infty}$ as a function of the tip–substrate distance normalized with respect to the radius *a*, of the tip. Above a conducting substrate (top curve), different sheath sizes exhibit no difference in tip current. Above an insulating substrate (bottom curves), different sheath sizes lead to different tip currents (the larger the sheath, the smaller the tip current). Reprinted with permission from ref. 66. Copyright 1990 American Chemical Society

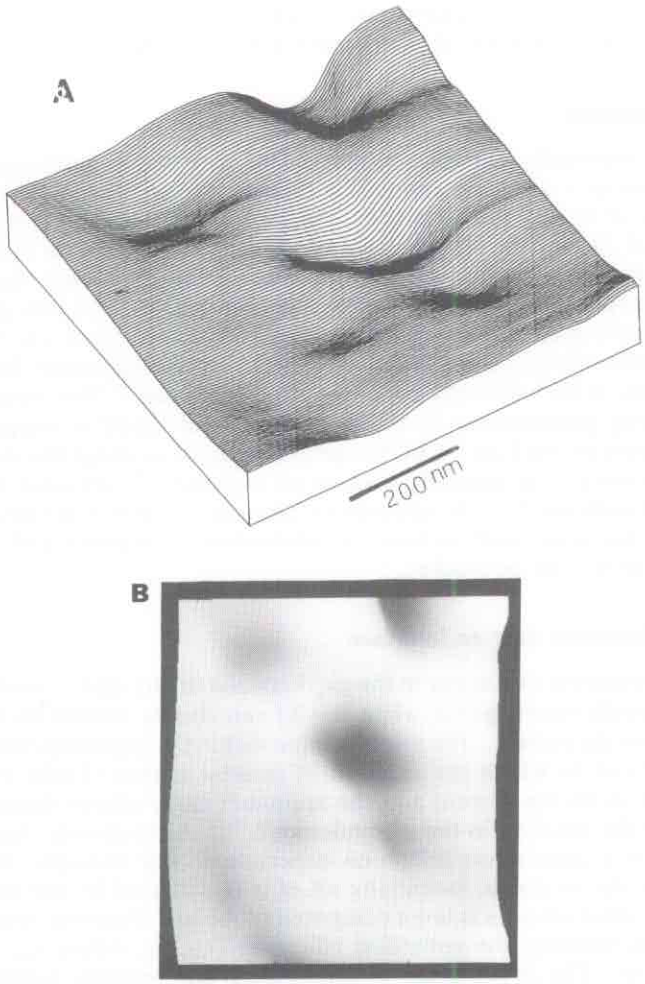

Fig. 18 720 nm × 650 nm constant-height SECM image of a Cyclopore polycarbonate membrane filter with nominal 0.2 μm pores. The solution contained 0.2 mol dm^{-3} $K_4Fe(CN)_6$ and 0.5 mol dm^{-3} $NaSO_4$. The tip potential was kept at 0.8 V *vs.* SCE. The rastering rate was 0.25 Hz. The current range is 0.15–0.45 nA. A, Topographic view. The image has been inverted, so the lower parts of the image represent the pore sites. B, Grey-scale image

(*e.g.* disk or cone) and on the rate constant, k° (cm s^{-1}), of the 'feedback' reaction $R \rightarrow O + ne$, at the substrate surface.[69] Typical limiting curves for $k^\circ \rightarrow 0$ and $k^\circ \rightarrow \infty$ for a disk-shaped tip encased in a narrow insulating sheath are given in Fig. 17. When k° is of an intermediate value, the relevant approach curves ($i_T/i_{T,\infty}$ *vs.* d/a) will lie between these limiting ones.[69,70] Thus the approach curve can be used to obtain k° and information about the rate of a reaction on the substrate below the tip and its nature. When the tip is scanned over the surface (in the x–y plane), the variations in tip current provide information about surface topography, and hence surface images, as well. The attainable x–y resolution depends upon the tip dimensions; an image of a polycarbonate membrane filter with nominal 0.2 μm pores is shown in Fig. 18. Surfaces that have been imaged by SECM include electrodes,[71] minerals,[72] membranes[73] and biological specimens.[74] In an alternative mode of operation, when the substrate of interest is an electrode, the tip

can be used in the collector (rather than the previously described feedback) mode. In this case species electrogenerated at the substrate are collected by the tip.[75]

Reaction Rate Imaging

The SECM is potentially capable of measuring very rapid heterogeneous electron-transfer reactions at a substrate surface by moving the tip close to the substrate. The maximum value of k° that can be determined is of the order of D/d, *e.g.* with a typical solution value of D and $d = 0.1\ \mu m$, a k° of *ca.* 1 cm s^{-1} should be attainable. Such a steady-state method has the advantage of not requiring short-time transient measurements and being free from problems associated with double-layer charging and adsorption of electroactive species. For example, we recently found the k° for electron transfer to C_{60} in *o*-dichlorobenzene–0.1 mol dm^{-3} tetra-*n*-butylammonium fluoroborate at a mercury electrode to be 0.46 ± 0.08 cm s^{-1} by this technique.[76] This measurement involved the interesting phenomenon in which a thin film of liquid is trapped when the tip penetrates the mercury surface.[77] SECM can also be used to image the areas on a surface where reactions occur, *e.g.* catalytic sites on an electrode,[78] corrosion sites, or enzyme locations in a membrane.[67,79] In addition to electron-transfer reactions, other types of heterogeneous reactions, such as rates of adsorption/desorption and surface protonation/deprotonation, can be studied.[72]

Homogeneous Reactions near an Interface

Homogeneous reactions that occur in the gap between the tip and a conductive substrate (*e.g.* for the example system given, when R → X) can also be studied by noting the effect of this reaction on the current. The small volume within the gap comprises an ultramicroelectrochemical cell in which the reaction of interest occurs (Table 1). The reaction causes a change in the tip current and the approach curve allows determination of the rate constant of the reaction in the ultramicrocell.[80,81] Alternatively, rate constants can be determined in a generation/collection experiment. For example, when species R, generated at the tip, is stable, essentially all of it is collected by the substrate when d is small and the substrate area is large compared to the tip. However, when R undergoes a decomposition reaction, the collection efficiency (i_{sub}/i_T, where i_{sub} is the substrate current) decreases. The dependence of i_{sub}/i_T on d and reactant concentration allows determination of the reaction rate and order. For example, the rapid dimerization of fumaronitrile ($k = 2 \times 10^5$ dm^3 mol^{-1} s^{-1}) was studied by this technique.[81] It may also be possible to study whether the homogeneous reactions are perturbed by the electric field near the surface by this technique, for example, by observing the effect of substrate potential on measured rate constant.

Table 1 Approximate volume, content and transit time of an ultramicrocell defined by an SECM tip (diameter, d) at a distance d from the substrate

		contents/molecules		
$d/\mu m$	V^a/cm^3	0.01 mol dm^{-3} solution	0.1 mol dm^{-3} solution	transit time τ^b/s
10	10^{-9}	4.5×10^9	4.5×10^{10}	0.1
1	10^{-12}	4.5×10^6	4.5×10^7	10^{-3}
0.1	10^{-15}	4500	4.5×10^4	10^{-5}
0.01	10^{-18}	4.5	45	10^{-7}

[a] $V = \pi d^3/4$, [b] $\tau \approx d^2/2D$.

Probing Interfacial Films

A potentially important application of SECM is as a means of studying thin films on interfaces. The investigation of films (*e.g.* polymers and self-assembled monolayers) at electrode surfaces has been the subject of many studies.[82] In most cases, characterization of the films and reactions that occur within them is carried out by macroscopic methods in which molecular and spatial information is obtained by comparing experimental results to predictions based on models. SECM can provide a more direct approach, *e.g.* to the measurement of film thickness *in situ*. For example, polyelectrolyte (Nafion) and electronically conductive polymer films have been investigated by SECM.[83-86] Consider the approach curve for a Nafion film containing $Os(bpy)_3^{2+}$ on a Pt substrate immersed in an electrolyte solution devoid of any electroactive species (Fig. 19).[83] When the conical tip is outside the film in the solution, only a negligible current flows. As soon as the tip contacts the film, current begins to flow as the reaction $Os(bpy)_3^{2+} \rightarrow Os(bpy)_3^{3+} + e$ occurs at the tip. The onset of current thus represents the film/solution boundary. The tip current increases as more of the tip enters the film, eventually attaining a constant value when the whole active tip surface is within the film. When the tip is within a distance of several tip diameters from the Pt, SECM positive feedback is seen and eventually i_T increases sharply because of tunnelling between the tip and Pt. The thickness of the film immersed in electrolyte, in the example 2200 Å, can be obtained directly from the approach curve without the assumptions and problems that may attend ellipsometric and profilometric determinations. Voltammetry can also be performed with the tip partially or completely within the film; a typical voltammogram is shown in Fig. 20. The shape of the voltammogram follows that expected for an ultramicroelectrode under steady-state mass-transfer conditions and allows estimation of values of D and $k°$. As with STM, one must be concerned about possible perturbations of the film

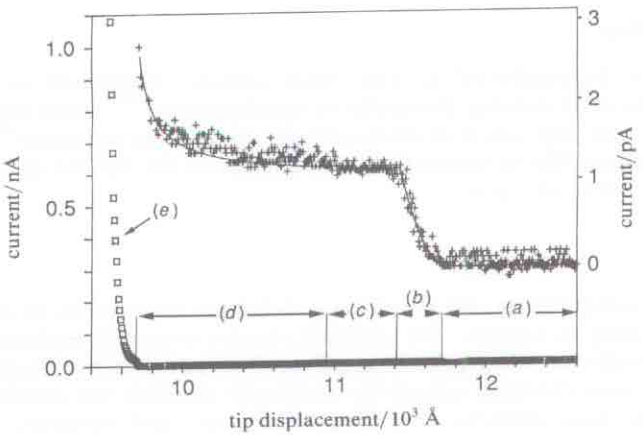

Fig. 19 Dependence of the tip current *vs.* distance: (*a*) tip outside film; (*b*) tip moving into film; (*c*) tip inside film; (*d*) onset of positive feedback; (*e*) onset of tunnelling. The displacement values are given with respect to an arbitrary zero point. The current observed during the stages (*a*)-(*d*) is much smaller than the tunnelling current and therefore cannot be seen on the scale of the lower curve (□) (the left-hand current scale). The upper curve (+) is at higher current sensitivity to show the current-distance curve corresponding to stages (*a*)-(*d*) (the right-hand current scale). The solid line is computed for a conical electrode with a height $h = 30$ nm and radius $r_0 = 30$ nm for zones (*a*)-(*c*) and SECM theory for zone (*d*). The tip was biased at 0.80 V *vs.* SCE, and the substrate was at 0.20 V *vs.* SCE. The tip moved at a rate of 30 Å s^{-1}. Reprinted with permission from ref. 83. Copyright 1992 American Association for the Advancement of Science

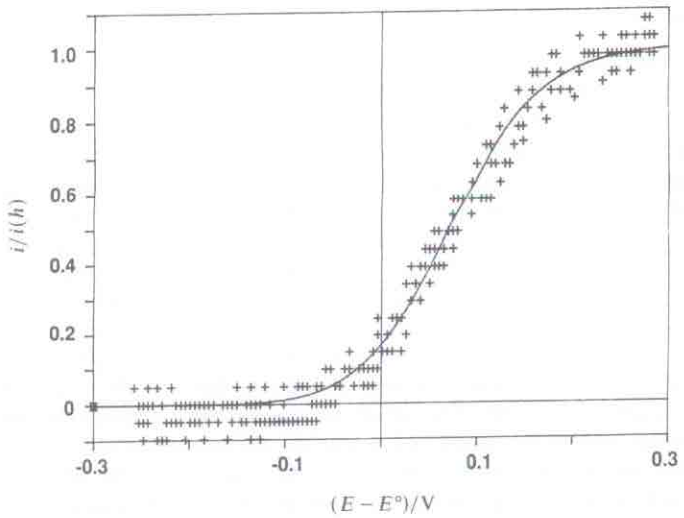

Fig. 20 Voltammogram at a microtip electrode partially penetrating a Nafion film containing 0.57 mol dm^{-3} Os $(bpy)_3^{2+}$. Scan rate $v = 5$ mV s^{-1}. The substrate was biased at 0.2 V *vs.* SCE. The solid line is the theoretical response with $D = 1.2 \times 10^{-9}$ cm^2 s^{-1} and $k° = 1.6 \times 10^{-4}$ cm s^{-1}. Reprinted with permission from ref. 83. Copyright 1992 American Association for the Advancement of Science

by the probing tip. This has not appeared to be a major problem with the small tip and the rather soft films described here.

SECM Fabrication

SECM can also be employed to alter solid surfaces immersed in liquids, *e.g.* by electrodeposition or by etching. Examples of metal plating,[87–90] metal and semiconductor etching,[88,89,91,92] and deposition of electronically conductive polymers[93] have appeared. The resolution attainable in fabrication is a function of the tip size and has so far been of the order of tenths of a μm.

Projections

SECM is still a rather young and developing technique and variations and new applications are continuing to appear. For example, we are currently exploring new types of tips, such as specific ion electrodes (*e.g.* pH probes) and enzyme electrodes.[79,94] These will allow improved chemical selectivity and make possible the probing of ion fluxes and distributions near surfaces, including membranes and minerals. Although most SECM studies have been based on steady-state measurements, transient approaches are also possible.[95] For example, diffusion coefficients and rate constants of homogeneous reactions can be measured by the time-of-flight between substrate and tip. Transient measurements could also be useful in the titration of surface sites or charge injection into surface states and traps. Finally, it should be possible to combine optical and electrochemical techniques in SECM. For example, by employing electrogenerated chemiluminescence (ECL) to produce excitation of surface species by tip-generated reactants, optical imaging with a resolution governed by the tip might be possible. Similarly, photochemical generation of species at the substrate with detection at the tip is possible. For example, we have recently studied the use of a semiconductor substrate (n-WSe_2) to photogenerate reactants that can be detected at the tip.[96]

Conclusions

Scanning probe techniques of various types, including STM, AFM and SECM, are undergoing rapid development and application. They continue to be promising methods for topographic imaging, determination of electronic distributions, and studying reactions at the liquid/solid interface with very high resolution.

The support of this research by grants from the US National Science Foundation (CHE9214480), Robert A. Welch Foundation and US Office of Naval Research is gratefully acknowledged.

References

1 A. J. Bard and L. R. Faulkner, *Electrochemical Methods*, Wiley, New York, 1980.
2 M. P. Soriaga, in *Progress in Surface Science*, ed. S. Davison, Pergamon, Oxford, in the press.
3 A. T. Hubbard, *Chem. Rev.*, 1988, **88**, 633.
4 K. Itaya, S. Sugawara, K. Sashikata and N. Furuya, *J. Vac. Sci. Technol.*, 1990, **A8**, 515.
5 S-L. Yau, C. M. Vitus and B. C. Schardt, *J. Am. Chem. Soc.*, 1990, **112**, 3677.
6 K. Sashikata, N. Furuya and K. Itaya, *J. Vac. Sci. Technol.*, 1991, **B9**, 457.
7 R. Christoph, H. Siegenthaler, H. Rohrer and H. Wiese, *Electrochim. Acta*, 1989, **34**, 1011.
8 M. Hopfner, W. Obretenov, K. Juttnev, W. J. Lorenz, G. Staikov, V. Bostanov and E. Budevski, *Surf. Sci.*, 1991, **248**, 225.
9 S-L. Yau, F-R. F. Fan, T. P. Moffat and A. J. Bard, to be submitted.
10 J. Wiechers, T. Twomey, D. M. Kolb and R. J. Behm, *J. Electoanal. Chem. Interfacial Electrochem.*, 1988, **248**, 451.
11 H. Honbo, S. Sugawara and K. Itaya, *Anal. Chem.*, 1990, **62**, 2424.
12 D. J. Trevor, C. E. D. Chidsey and D. N. Loiacono, *Phys. Rev. Lett.*, 1989, **62**, 929.
13 E. Holland-Moritz, J. Gordon II, G. Borges and R. Sonnenfeld, *Langmuir*, 1991, **7**, 301.
14 X. Gao, A. Hamelin and M. J. Weaver, *J. Chem. Phys.*, 1991, **95**, 6993.
15 X. Gao, A. Hamelin and M. J. Weaver, *Phys. Rev. B*, 1991, **44**, 10983.
16 R. Sonnenfeld and P. K. Hansma, *Science*, 1986, **232**, 211.
17 A. A. Gewirth and A. J. Bard, *J. Phys. Chem.*, 1988, **92**, 5363.
18 H. Chang and A. J. Bard, *Langmuir*, 1991, **7**, 1143.
19 H. Chang and A. J. Bard, *J. Am. Chem. Soc.*, 1990, **112**, 4598.
20 H. Chang and A. J. Bard, *J. Am. Chem. Soc.*, 1991, **113**, 5588.
21 S. E. Gilbert and J. H. Kennedy, *J. Electrochem. Soc.*, 1988, **135**, 2385.
22 K. Itaya and E. Tomita, *Chem. Lett.*, 1989, 285.
23 K. Sakamaki, K. Itoh, A. Fujishima and Y. Gohshi, *J. Vac. Sci. Technol.*, 1990, **A8**, 614.
24 F-R. F. Fan and A. J. Bard, *J. Phys. Chem.*, 1990, **94**, 3761.
25 K. Itaya and E. Tomita, *Surf. Sci.*, 1989, **219**, L515.
26 P. Carlsson, B. Holmstrom, H. Kita and K. Uosaki, *J. Electroanal. Chem. Interfacial Electrochem.*, 1990, **283**, 425.
27 R. Sonnenfeld, J. Schneir, B. Draker, P. K. Hansma and D. E. Aspnes, *Appl. Phys. Lett.*, 1987, **50**, 1742.
28 T. Thundat, L. A. Nagahara and S. M. Lindsay, *J. Vac. Sci. Technol.*, 1990, **A8**, 539.
29 F-R. F. Fan and A. J. Bard, *J. Phys. Chem.*, 1991, **95**, 1969.
30 E. Tomita, N. Matsuda and K. Itaya, *J. Vac. Sci. Technol.*, 1990, **A8**, 534.
31 R. Houbertz, U. Memment and R. J. Behm, *Appl. Phys. Lett.*, 1991, **58**, 1027.
32 H. E. Hessel, A. Feltz, M. Reiter, U. Memment and R. J. Behm, *Chem. Phys. Lett.*, 1991, **186**, 275.
33 S-L. Yau, F-R. F. Fan and A. J. Bard, *J. Electrochem. Soc.*, 1992, **139**, 2825.
34 K. Itaya, S. Sugawara, Y. Morita and H. Tolumoto, *Appl. Phys. Lett.*, 1992, **60**, 2534.
35 R. S. Becker, G. S. Higashi, Y. J. Chabal and A. J. Becker, *Phys. Rev. Lett.*, 1990, **65**, 1917.
36 Y. Kim and C. M. Lieber, *J. Am. Chem. Soc.*, 1991, **113**, 2333.
37 B. Parkinson, *J. Am. Chem. Soc.*, **112**, 7498.
38 N. Casillas, S. R. Snyder, W. H. Smyrl and H. S. White, *J. Phys. Chem.*, 1991, **95**, 7002.
39 J. A. Stroncio, R. M. Feenstra, D. M. Newns and A. P. Fein, *J. Vac. Sci. Technol.*, 1988, **A6**, 499.
40 D. M. Kolb, in *Advances in Electrochemistry and Electrochemical Engineering*, ed. H. Gerischer and C. W. Tobias, Wiley, New York, 1984, vol. 11, pp. 125–271.
41 M. P. Green, K. J. Hanson, R. Carr and I. Lindau, *J. Electrochem. Soc.*, 1990, **137**, 3493.
42 K. Sashikata, N. Furuya and K. Itaya, *J. Electroanal. Chem. Interfacial Electrochem.*, 1991, **316**, 361.
43 O. M. Magnussen, J. Hetlos, R. J. Nichols, D. M. Kolb and R. J. Behm, *Phys. Rev. Lett.*, 1990, **64**, 2929.
44 T. Hachiya, H. Honbo and K. Itaya, *J. Electroanal. Chem. Interfacial Electrochem.*, 1991, **315**, 275.
45 S. Manne, P. K. Hansma, J. Massie, V. B. Elings and A. A. Gewirth, *Science*, 1991, **251**, 183.

46 B. C. Schardt, S-L. Yau and F. Rinelli, *Science*, 1989, **243**, 1050.
47 S-L. Yau, X. Gao, S-C. Chang, B. C. Schardt and M. J. Weaver, *J. Am. Chem. Soc.*, 1991, **113**, 6049.
48 C. M. Vitus, S-C. Chang, B. C. Schardt and M. J. Weaver, *J. Phys. Chem.*, 1991, **95**, 7559.
49 C. A. Widrig, C. A. Alves and M. C. Porter, *J. Am. Chem. Soc.*, 1991, **113**, 2805.
50 L. Haussling, B. Michel, H. Ringsdorf and H. Rohrer, *Angew. Chem., Int. Ed. Engl.*, 1991, **30**, 569.
51 D. P. E. Smith, A. Bryant, C. F. Quate, J. P. Rabe, Ch. Gerber and J. D. Swalen, *Proc. Natl. Acad. Sci. USA*, 1987, **844**, 969.
52 D. P. E. Smith, J. K. H. Hober, Ch. Gerber and G. Binning, *Science*, 1989, **245**, 43.
53 D. P. E. Smith, J. K. H. Hober, G. Binning and H. Nehoh, *Nature (London)*, 1990, **344**, 641.
54 R. L. McCarley and A. J. Bard, *J. Phys. Chem.*, 1991, **95**, 9618.
55 B. G. Bravo, S. L. Micelhaugh, M. P. Soriaga, I. Villegas, D. W. Suggs and J. L. Stickney, *J. Phys. Chem.*, 1991, **95**, 5245.
56 R. L. McCarley, Y-T. Kim and A. J. Bard, *J. Phys. Chem.*, in the press.
57 R. L. McCarley, Y-T. Kim and A. J. Bard, *J. Phys. Chem.*, 1992, **96**, 7416.
58 Y-T. Kim and A. J. Bard, *Langmuir*, 1992, **8**, 1096.
59 Y-T. Kim and A. J. Bard, *Langmuir*, submitted.
60 S. A. Hendricks, Y-T. Kim and A. J. Bard, *J. Electrochem. Soc.*, 1992, **139**, 2818.
61 R. L. McCarley and A. J. Bard, *J. Phys. Chem.*, 1992, **96**, 7410.
62 T. P. Moffat, F-R. F. Fan and A. J. Bard, *J. Electrochem. Soc.*, 1991, **138**, 3224.
63 I. C. Oppenheim, D. J. Trevor, C. E. D. Chidsey, P. L. Trevor and K. Sieradzki, *Science*, 1991, **254**, 687.
64 C. F. Quate, in *Scanning Tunnelling Microscopy and Related Methods*, R. J. Behm, N. Garcia and H. Rohrer, Kluwer Academic Publishers, Dordrecht, 1990, NATO ASI Series, Series E: Applied Sciences, vol. 184, pp. 281–297.
65 C-Y. Liu and A. J. Bard, *Chem. Phys. Lett.*, 1990, **174**, 162.
66 A. J. Bard, G. Denuault, C. Lee, D. Mandler and D. O. Wipf, *Acc. Chem. Res.*, 1990, **23**, 357.
67 A. J. Bard, F-R. F. Fan, D. T. Pierce, P. R. Unwin, D. O. Wipf and F. Zhou, *Science*, 1991, **254**, 68.
68 A. J. Bard, F-R. Fan, M. Mirkin, *Electroanalytical Chemistry*, ed. A. J. Bard, Dekker, New York, 1993, in the press.
69 D. O. Wipf and A. J. Bard, *J. Electrochem. Soc.*, 1991, **138**, 469.
70 M. V. Mirkin and A. J. Bard, *J. Electroanal. Chem.*, 1992, **323**, 1.
71 A. J. Bard, F-R. F. Fan, J. Kwak and O. Lev. *Anal. Chem.*, 1989, **61**, 132.
72 P. R. Unwin and A. J. Bard, *J. Phys. Chem.*, 1992, **96**, 5035.
73 E. R. Scott, H. S. White and J. B. Phillips, *J. Membr. Sci.*, 1991, **58**, 71.
74 C. Lee, J. Kwak and A. J. Bard, *Proc. Natl. Acad. Sci. USA*, 1990, **87**, 1740.
75 R. C. Engstrom, T. Meany, R. Tople and R. M. Wightman, *Anal. Chem.*, 1987, **59**, 2005.
76 M. Mirkin, L. O. S. Bulhões and A. J. Bard, *J. Am. Chem. Soc.*, in the press.
77 M. Mirkin and A. J. Bard, *J. Electrochem. Soc.*, 1992, **139**, 3535.
78 D. O. Wipf and Allen J. Bard, *J. Electrochem. Soc.*, 1991, **138**, L4.
79 D. T. Pierce and A. J. Bard, to be submitted.
80 P. R. Unwin and A. J. Bard, *J. Phys. Chem.*, 1991, **95**, 7814.
81 F. Zhou, P. R. Unwin and A. J. Bard, *J. Phys. Chem.*, 1992, **96**, 4917.
82 *Molecular Design of Electrode Surfaces*, ed. R. M. Murray, Wiley–Interscience, New York, 1992.
83 M. Mirkin, F-R. Fan and A. J. Bard, *Science*, 1992, **257**, 364.
84 J. Kwak, C. Lee and A. J. Bard, *J. Electrochem. Soc.*, 1990, **137**, 1481.
85 C. Lee and A. J. Bard, *Anal. Chem.*, 1990, **62**, 1906.
86 C. Lee, J. Kwak and F. C. Anson, *Anal. Chem.*, 1991, **63**, 1501.
87 D. H. Craston, C. W. Lin and A. J. Bard, *J. Electrochem. Soc.*, 1988, **135**, 785.
88 O. E. Hüsser, D. H. Craston and A. J. Bard, *J. Vac. Sci. Technol.*, 1988, **B6**, 1873.
89 O. E. Hüsser, D. H. Craston and A. J. Bard, *J. Electrochem. Soc.*, 1989, **136**, 3222.
90 D. Mandler and A. J. Bard, *J. Electrochem. Soc.*, 1990, **137**, 1079.
91 C. W. Lin, F-R. F. Fan and A. J. Bard, *J. Electrochem. Soc.*, 1987, **134**, 1038.
92 D. Mandler and A. J. Bard, *J. Electrochem. Soc.*, 1990, **137**, 2468.
93 Y-M. Wuu, F-R. F. Fan and A. J. Bard, *J. Electrochem. Soc.*, 1989, **136**, 885.
94 B. Horrocks, M. V. Mirkin, D. T. Pierce, A. J. Bard, G. Nagy and K. Toth, *Anal. Chem.*, submitted.
95 A. J. Bard, G. Denuault, R. A. Friesner, B. C. Dornblaser and L. S. Tuckerman, *Anal. Chem.*, 1991, **63**, 1282.
96 F. Fan and A. J. Bard, *J. Phys. Chem.*, in the press.

Paper 2/05507D; *Received* 12*th October*, 1992